Journal Pre-proof

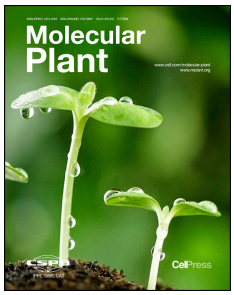

Sucrose-responsive osmoregulation of plant cell size by a long non-coding RNA

Jakub Hajný, Tereza Trávníčková, Martina Špundová, Michelle Roenspies, R. M. Imtiaz Karim Rony, Sebastian Sacharowski, Michal Krzyszton, David Zalabák, Christian S. Hardtke, Aleš Pečinka, Holger Puchta, Szymon Swiezewski, Jaimie M. van Norman, Ondřej Novák

PII: S1674-2052(24)00300-9

DOI: https://doi.org/10.1016/j.molp.2024.09.011

Reference: MOLP 1792

To appear in: *MOLECULAR PLANT*

Received Date: 8 July 2024

Revised Date: 10 September 2024

Accepted Date: 26 September 2024

Please cite this article as: Hajný J., Trávníčková T., Špundová M., Roenspies M., Karim Rony R.M.I., Sacharowski S., Krzyszton M., Zalabák D., Hardtke C.S., Pečinka A., Puchta H., Swiezewski S., van Norman J.M., and Novák O. (2024). Sucrose-responsive osmoregulation of plant cell size by a long non-coding RNA. Mol. Plant. doi: https://doi.org/10.1016/j.molp.2024.09.011.

Sucrose-responsive osmoregulation of plant cell size by a long non-coding RNA

Jakub Hajný[1]*, Tereza Trávníčková[1], Martina Špundová[2], Michelle Roenspies[3], R. M. Imtiaz Karim Rony[4], Sebastian Sacharowski[5], Michal Krzyszton[5], David Zalabák[1], Christian S. Hardtke[6], Aleš Pečinka[7], Holger Puchta[3], Szymon Swiezewski[5], Jaimie M. van Norman[4] and Ondřej Novák[1]

*Corresponding author: Jakub Hajný, jakub.hajny@upol.cz

Affiliations

[1] Laboratory of Growth Regulators, The Czech Academy of Sciences, Institute of Experimental Botany and Palacky University, Slechtitelu 27, CZ-77900 Olomouc Czech Republic

[2] Department of Biophysics, Faculty of Science, Palacky University, Slechtitelu 27, CZ-77900 Olomouc, Czech Republic

[3] Joseph Gottlieb Kölreuter Institute for Plant Sciences (JKIP) – Molecular Biology, Karlsruhe Institute of Technology, Karlsruhe, Germany

[4] Department of Molecular, Cell, and Developmental Biology, University of California, Los Angeles, CA 90095

[5] Laboratory of Seeds Molecular Biology, Institute of Biochemistry and Biophysics Polish Academy of Sciences, Pawinskiego 5a, 02-106 Warsaw, Poland

[6] Department of Plant Molecular Biology, University of Lausanne, Lausanne, Switzerland

[7] Centre of Plant Structural and Functional Genomics, Institute of Experimental Botany, Czech Acad Sci, Šlechtitelů 31, CZ-77900 Olomouc, Czech Republic

Short Summary

The CARMA-CANAR module acts as a novel osmoregulatory system controlling cell size in the root stele in response to external osmolality. CANAR activity regulates the shoot-to-root phloem transport of sugars, which influences internal pressure via cellular water uptake and, thus, resultant cell size.

Abstract

In plants, sugars are the key source of energy and metabolic building blocks. The systemic transport of sugars is essential for plant growth and morphogenesis. Plants evolved intricate molecular networks to effectively distribute sugars. The dynamic distribution of these osmotically active compounds is a handy tool for regulating cell turgor pressure, an instructive force in developmental biology. Here, we set out to investigate the molecular mechanism behind the dual role of a receptor-like kinase CANAR. We functionally characterized a long non-coding RNA, *CARMA*, as a negative regulator of CANAR. Sugar-responsive *CARMA* specifically fine-tunes *CANAR* expression in the phloem, the route of sugar transport. Based on our genetics, molecular, microscopy, and biophysical data, we propose that by controlling sugar phloem transport from shoot to root, the CARMA-CANAR module allows cells to flexibly adapt to the external osmolality by appropriate water uptake and thus adjust the size of vascular cell types during organ growth and development. We identify a nexus of plant vascular tissue formation with cell internal pressure monitoring and reveal a novel functional aspect of long non-coding RNAs in developmental biology.

Introduction

In contrast to the circulatory vascular system of vertebrates, plants evolved non-circulatory specialized vascular bundles with two distinct long-distance transport routes. The xylem is a unidirectional root-to-shoot path for the transport of water and minerals from the soil. The phloem route transports carbon assimilates, amino acids, RNAs, and hormones from source tissues (e.g. mature leaves) into sink tissues (such as juvenile leaves, roots, meristems, and reproductive organs) (Fukuda and Ohashi-Ito, 2019; Hardtke, 2023). The hydrostatic pressure differences between source and sink drive the flow of the phloem content (Knoblauch et al., 2016). In most plants, sucrose is the main form of assimilated carbon from photosynthesis, making it the central metabolite in plant growth and development. Sucrose is synthesized from fructose and glucose in photosynthetically active cells. Plants favor non-reducing sugar sucrose since high concentrations of reducing sugars can non-enzymatically glycosylate essential proteins and interfere with their functionality (Geiger, 2020). In apoplasmically loading plants like Arabidopsis, sucrose export from photosynthetic cells (mesophyll in leaves) to the apoplast is facilitated by SUGARS WILL EVENTUALLY BE EXPORTED TRANSPORTERS (SWEETs) efflux proteins. Then, sucrose enters the phloem via SUCROSE TRANSPORTERs (SUCs), a process termed apoplastic phloem loading. SUCs are H^+/sucrose symporters, loading sucrose against its concentration gradient. Sucrose is unloaded from the phloem in sink tissues and distributed via SWEET proteins. Sink tissues either store sucrose in vacuoles or convert it back to glucose and fructose by invertase enzymes. Ultimately, the sugars are consumed or stored in vacuoles (Julius et al., 2017; Geiger, 2020).

Plant growth involves physical remodeling of cell wall mechanics and cell hydrostatic pressure. Plant cells have a high intracellular hydrostatic pressure, called turgor pressure, which

results from water uptake in response to the solute concentration (e.g. ions and sugars) and is counterbalanced by the rigid yet dynamic cell walls (Cosgrove, 2016; Ali et al., 2023). If osmotic conditions change, plant cells regulate water and ion transport across the plasma membrane (PM) and remodel their cell wall to compensate for the turgor pressure difference. The balance between turgor pressure and cell wall tension at the cell level translates to the tissue level, driving tissue patterning. These mechanical forces play an instructive role in developmental biology across kingdoms. For example, accumulating evidence suggests that in the shoot, the epidermis possesses thicker cell walls, providing a high resistance pillar for aerial organ development. In the root, the endodermis likely plays a similar role as the epidermis in the shoot. Both internal turgor pressure and external mechanical perturbations can alter cell size, geometry, polarity, cell division plane orientations, and, thus, finally shape the plant body (Hamant and Haswell, 2017).

In the *Arabidopsis thaliana* root, INFLORESCENCE AND ROOT APICES RECEPTOR KINASE (IRK), a leucine-rich repeat receptor-like kinase (LRR-RLK) regulates stele (i.e., the vascular cylinder surrounded by the pericycle layer) size, and restricts excessive endodermal cell divisions (Campos et al., 2020). IRK's closest homolog PXY/TDR-CORRELATED 2 (PXC2), also called CANALIZATION-RELATED RECEPTOR-LIKE KINASE (CANAR), exerts an overlapping, partially redundant function despite not being expressed in the same tissues (Goff et al., 2023). Both IRK and CANAR/PXC2 were recently reported to contribute to vascular patterning via auxin canalization (Hajný et al., 2020; Goff et al., 2023). Interestingly, the relative number of cells in the stele between wild-type (WT) and *CANAR* mutant/overexpressor lines are similar despite the significant change in root stele area (Goff et al., 2023). This suggests mechanical remodelling, which, ultimately, alters cell volume instead of cell number. How CANAR participates in cell volume adjustment remains unknown. We propose that the missing link is the fine-tuning of systemic sugar transport.

Long non-coding RNAs (lncRNAs) are essential regulatory elements of eukaryotic transcriptomes. lncRNAs are versatile regulators of gene expression, functioning at different cellular levels, often providing adaptive mechanisms to various stimuli (Wang and Chang, 2011). Only a handful of lncRNAs have been functionally characterized and implicated in aspects of plant development (Chorostecki et al., 2023). In this study, we characterized a newly annotated lncRNA, *CARMA* (*CANAR MODULATOR IN PROTOPHLOEM*), which is located in the proximal promoter region of *CANAR* in *Arabidopsis thaliana* genome. *CARMA* fine-tunes the phloem-specific expression of *CANAR* in response to sucrose availability. Tightly controlled *CANAR* levels in the phloem are required for optimal shoot-to-root sugar transport to adjust cell turgor and, thus, stele cell size in response to the environment.

Results

Newly annotated antisense long non-coding RNA is located in the *CANAR* proximal promoter

We set out to unravel the molecular mechanisms regulating CANAR activity by re-examining its expression pattern. Previously, the transcriptional reporter, consisting of the entire intergenic region (4.7 kbp) upstream of the *CANAR* start codon with an ER-targeted green fluorescent protein (*pCANAR::erGFP)* showed weak activity in the Arabidopsis root tip (Goff et al., 2023). To observe a more native expression pattern, we rebuilt the reporter by adding the 3' untranslated region (UTR) downstream of the *CANAR* stop codon to nuclear-targeted GFP and β-glucuronidase (*pCANAR::NLS-GFP-GUS-ter*). This reporter exhibited a markedly stronger fluorescent signal, localized mainly to the lateral root cap (LRC) and xylem (X), corresponding with the previous report (Goff et al., 2023). Lower expression could also be seen in the root phloem precursors: developing protophloem sieve elements (PPh) and metaphloem (MPh) (Figure 1A). β-glucuronidase staining recapitulated previous observations (Wang et al., 2013), showing expression throughout the seedling vasculature. Staining in the first leaves occurred at the position of the future vasculature strands (Figure 1B), supporting the previously described role of CANAR in vascular patterning via auxin canalization (Hajný et al., 2020). We attribute the stronger expression of the novel reporter to the presence of the 3' UTR, possibly stabilizing the *CANAR* transcripts.

During the design of *pCANAR* reporter, we noticed a newly annotated 353 bp antisense long non-coding RNA (lncRNA) (AT5G00810) in the proximal promoter region of *CANAR*, partially overlapping with its 5' UTR (Figure 1C). We hypothesized that this lncRNA, named *CARMA* (*CANAR MODULATOR IN PROTOPHLOEM*), might help us understand the relationship between tissue-specific expression of *CANAR* and its developmental functions. Using a semi-quantitative Reverse Transcription Polymerase Chain Reaction (sqRT-PCR), we confirmed that *CARMA* is expressed in seedlings and that the transcript is presumably polyadenylated as it could be amplified from oligo dT primed cDNA (Figure 1D). We performed 5' and 3' Rapid Amplification of cDNA Ends (RACE) to define the full-length *CARMA* transcript. The transcription start site (TSS) largely matched annotation, whereas the 3' end has several transcription termination sites (TTS). The annotated length of 353 bp constituted ~50% of all *CARMA* transcripts with a maximum detected transcript length of 491 bp (Supplemental Figure S1A, B).

A transcriptional reporter containing 5 kb upstream of *CARMA* fused with *NLS-GFP-GUS* (*pCARMA(5kb)::NLS-GFP-GUS*), revealed *CARMA* promoter activity in the PPh with occasional expression in MPh. Additionally, in the meristematic zone, a shootward gradient of weaker expression in the xylem was also observed (Figure 1E, F and Supplemental Figure 1C). The activity of *pCARMA* in the xylem was not seen with a shortened version of the promoter (*pCARMA(1.3kb)::NLS-GFP-GUS*) (Supplemental Figure 1D, E). Similar to *pCANAR*, *pCARMA* activity in the first leaves occurred at the position of the future vasculature strands, a manifestation of auxin canalization (Scarpella et al., 2006) (Figure 1F). Thus, *pCANAR* and *pCARMA* have overlapping patterns of activity, but their intensity profiles are inverse, suggesting a possible role for *CARMA* in transcriptional regulation of *CANAR*.

CARMA controls leaf vascular patterning

CARMA expression in the cotyledons and first leaves prompted us to test the involvement of *CARMA* in leaf vascular patterning, a proxy for auxin canalization (Scarpella et al., 2006). We isolated an available T-DNA insertion loss-of-function mutant (*carma-1*) (Supplemental Figure 2A, B). Because the *carma-1* T-DNA insertion is close to the *CANAR* 5' UTR (Supplemental Figure 2A), we tested whether it affects *CANAR* transcription. *CANAR* mRNA levels were slightly elevated (Supplemental Figure 2C), excluding the possibility of T-DNA-mediated knock-down of *CANAR*. Next, we generated transgenic lines overexpressing *CARMA* under the control of the constitutive cauliflower mosaic virus *35S* promoter (Supplemental Figure 2D). Two independent *35S::CARMA* overexpression lines showed a higher incidence of extra vascular loops, extra branches, and disconnections in the upper loops as compared to the wildtype (Col-0) control (Figure 2A, B). These higher complexity venation phenotypes resembled that of *canar* mutants (Hajný et al., 2020). In contrast, *carma-1* plants exhibited simpler venation, indicated by missing loops (Figure 2C, D), similar to *35S::CANAR-GFP* (Hajný et al., 2020).

The inverse intensity of *pCANAR* and *pCARMA* activity in the X/PPh and the opposite vein patterning phenotypes indicate that *CARMA* is a negative regulator of *CANAR* activity.

CARMA mediates cell size changes in response to media osmolality in the stele

Whereas *canar-3* roots had an enlarged stele area, *CANAR* overexpression had the opposite effect. The stele area difference was due to a change in cell size and not cell number. This phenotype was conditional, manifested only in more hypotonic growth conditions where the agar plates contained 0.2x strength Murashige and Skoog medium (MS) basal salts media (Goff et al., 2023), suggesting an involvement of internal water pressure in the *CANAR* phenotype. Thus, we tested whether *CARMA* also plays a role in stele area control on media with different osmolality (0.2x, 0.5x, and 1x MS). As *35S* promoter activity is weak in the root meristem vasculature, we overexpressed *CARMA* under the β-estradiol inducible promoter (Zuo et al., 2000) (*XVE>>CARMA)* (Supplemental Figure 2E). After β-estradiol treatment from germination onward, we observed a significantly enlarged stele area on 0.2x MS in two independent *XVE>>CARMA* lines compared to the Mock controls (Figure 2E, G). Similar to what has been observed for *canar* mutants (Goff et al., 2023). Conversely, the *carma-1* roots exhibited a smaller stele area than WT, but only on 1x MS media (Figure 2F, H), analogous to but weaker than *XVE>>CANAR* overexpression stele phenotype (Goff et al., 2023). Again, no change in the vascular cell number was observed (Supplemental Figure 2G, H and 3A, B), indicating the difference in stele area can be attributed to altered cell size, not proliferation. By measuring the distance from the endodermis to the lateral root cap, we confirmed that cell expansion is specific to the stele (Supplemental Figure 2F and 3C). Also, no change in root meristem length was observed (Supplemental Figure 2I, J and 3D, E), indicating that the stele area phenotype is not the result of changes in differentiation.

To this end, our results suggest that *CARMA* is a negative regulator of *CANAR.* A cross of *canar-3* mutant with *XVE>>CARMA* overexpressing line could not further enhance the *canar-3* stele area phenotype on 0.2x MS medium (Supplemental Figure 2K), proving *CANAR* is a primary target of *CARMA*. Given the close proximity of the T-DNA cassette of *carma-1* and *canar-3* mutants, a successful generation of double mutant via crossing is not possible. Hence, we opted for CRISPR/Cas9-mediated deletion of the *CARMA* locus and part of the first exon of *CANAR* (Supplemental Figure 3F, G). We obtained two independent lines, which we named *canar-4 C2* and *canar-4 C4*. Both mutants showed no rescue on 0.2x MS, placing *CARMA* upstream of the CANAR function (Supplemental Figure 2L).

The conditional nature of these stele area phenotypes indicates a dependence on the osmolality of the media. Because the *canar-3* mutant has an enlarged stele on hypotonic media, we hypothesized that stele cells might retain excess water, making them bulkier. If true, lowering the intracellular water content would revert the phenotype. To test this hypothesis, we decided to use mannitol, an osmotically active sugar that cannot penetrate the PM (Hohl and Schopfer, 1991) and, therefore, reduce cellular water content. To isolate the effect of osmolality from other effects, such as nutrient level, we measured the osmolality of 0.2x MS (29 mOsm/kg) and 1x MS (95 mOsm/kg) media and then supplemented 0.2x MS medium with mannitol to match the osmolality of 1x MS (Supplemental Table 1). The needed mannitol concentration was approximately 64 mM. Indeed, the *canar-3* mutant phenotype was reverted on 0.2x MS media with 64 mM mannitol (Supplemental Figure 2M). A similar effect was observed for *XVE>>CARMA* (Supplemental Figure 2N), while Col-0 could compensate for the osmolality change normally (Supplemental Figure 2O).

CARMA fine-tunes *CANAR* expression in the root protophloem

The antisense orientation of *CARMA*, its inverse intensity expression profile in the X/PPh, and opposite leaf vasculature and stele area phenotypes with respect to *CANAR* imply that *CARMA* is a negative regulator of *CANAR*. To understand how *CARMA* influences CANAR function, we generated a set of transcriptional reporters consisting of the full-length 4.7 kbp *CANAR* promoter-*pCANAR::NLS-GFP-GUS-ter*, a partial deletion of *CARMA*- *pCANAR_CARMAΔ::NLS-GFP-GUS-ter*, and complete deletion of *CARMA* (removing part of the *CANAR* 5' UTR as well)-*pCANAR_CARMAΔΔ::NLS-GFP-GUS-ter* (Figure 3A), transformed into *carma-1* mutant background. Using confocal microscopy, we observed that both deletions resulted in a significant, tissue-specific increase of *pCANAR* activity in the PPh to a level comparable to X. The insertional character of these transgenic lines does not allow absolute quantification; therefore, we opted for relative quantification of the PPh/X ratio of the fluorescence signal. Two independent transgenic lines were analyzed for each reporter (Figure 3A, B and Supplemental Figure 4A, B). The similar outcomes of the *CARMAΔ* and *CARMAΔΔ* deletions confirmed that changes in *pCANAR* activity are not due to an indirect impact of its partial 5' UTR deletion. In line with our observations, the *carma-1* mutant had increased (Supplemental Figure 2C), and *35S::CARMA* overexpression

decreased *CANAR* levels (Supplemental Figure 4C). Modest changes in *CANAR* expression reflect a smaller pool of protophloem cells compared to the xylem one.

Our results demonstrate that *CARMA* modulates *CANAR* levels to establish a differential of high *CANAR* expression in X and low in PPh. To address the biological significance of this stringent PPh-specific fine-tuning mechanism, we expressed *CANAR* either ubiquitously or tissue-specifically in the PPh. We utilized an *XVE>>CANAR-3xHA* line, which inducibly overexpresses *CANAR*, causing a marked decrease in the stele area (Goff et al., 2023). We could elicit this phenotype on 1x MS medium (Figure 3C, D), where the *carma-1* plants exhibited a smaller stele area as well (Figure 2F, H). Next, we generated *pCVP2>>XVE::CANAR-GFP-ter*, allowing for protophloem-specific inducible overexpression of *CANAR* (Fandino et al., 2023). These transgenic plants grown on β-estradiol showed protophloem-specific GFP fluorescence (Figure 3C) and had significantly decreased stele area, although not to the extent of *XVE>>CANAR-3xHA* (Figure 3D). This effect was not observed on 0.5x and 0.2x media, although *XVE>>CANAR-3xHA* had variable stele area on 0.2x MS media without a reproducible trend across all replicates (Supplemental Figure 4D, E). This could mean that either the xylem-expressed *CANAR* is also involved in this process or it is a consequence of *CANAR* misexpression. Alternatively, the phenotypic difference might be due to the missing *CANAR* expression in MPh when the *CVP2* (*COTYLEDON VASCULAR PATTERN 2*) promoter is used.

Our results suggest that fine-tuned levels of *CANAR* in the PPh are required for the cell size adjustment in response to changes in external osmolality and are, thus, required for the optimization of stele area.

CARMA mediates *CANAR* responsivity to sucrose

To better understand the CANAR function, we set out to analyze the translational fusion of CANAR driven by its native promoter (*pCANAR::CANAR-GFP)* (Goff et al., 2023). Since the expression was too weak, we deployed a similar approach as with the *pCANAR::NLS-GFP-GUS-ter* transcriptional reporter, where the addition of the *CANAR* 3' UTR enhanced the fluorescence signal. Indeed, *pCANAR::CANAR-GFP-ter* provided a stronger signal (Supplemental Figure 5A). Except for the PM, a vesicular signal in the cytoplasm could also be observed, suggesting dynamic subcellular trafficking of CANAR. We noticed that fluorescence intensity and PM-localized signal in two independent transgenic lines depended on the presence of sucrose in the growth media (Supplemental Figure 5A). Glucose exerted a similar effect, which was not observed after treatment with mannitol (Figure 4A and Supplemental Figure 5B), NaCl (Supplemental Figure 5C), or changing the media osmolality (0.2x, 0.5x, and 1x MS) (Supplemental Figure 5D). Three-fold higher sucrose concentration did not stimulate additional accumulation of CANAR (Figure 4A and Supplemental Figure 5B), indicating a maximum threshold. To further uncouple the effect of sugar from the osmotic pressure, we tested if sucrose-mediated CANAR upregulation can be rescued by a cotreatment with mannitol, which should compete with sucrose for intracellular water and thus alleviate the internal pressure. Mannitol did not change the sucrose responsivity of

CANAR (Figure 4A and Supplemental Figure 5B). The same observations were also made for *pCARMA(5kb)::NLS-GFP-GUS* transgenic line (Supplemental Figure 6A).

Next, we tested if CANAR expression in the root could respond to sugars transported from the shoot. Plants were grown on 0.5x MS medium without sucrose for five days, and then the shoots were placed on a glass cover lid to separate them from the media. Shoots were exposed to liquid 0.5x MS medium alone or containing sucrose or glucose. After five hours, we observed CANAR upregulation in the root upon sucrose and glucose application (Figure 4B, C).

Increased CANAR accumulation in the root upon exposure to sucrose is, at least partially, explained by increased *CANAR* mRNA levels in both leaves and roots (Figure 4D, E). In leaves, *CANAR* response was transient, peaking at 0.5 to 1h, and then it was gradually lost. In roots, sucrose-mediated *CANAR* upregulation peaked at 2h, and then it slightly decreased to levels maintained throughout the tested time window. *CARMA* followed a similar trend in both tissues (Figure 4D, E). In the *carma-1* mutant, *CANAR* sensitivity to sucrose was elevated both in leaves and roots (Figure 4F, G), whereas overexpression of *CARMA* did not show any effect in tested conditions (Figure 4H, I). Mannitol did not affect *CARMA* and *CANAR* expression (Supplemental Figure 5E, F).

In summary, sucrose upregulates both *CANAR* and *CARMA* expression in an akin temporal manner. The upregulation is specific to PM-permeable sugars since using other osmotically active molecules did not mimic this effect. *CARMA* changes the *CANAR* sensitivity to sucrose.

The CARMA-CANAR module regulates the shoot-to-root transport of sugars

The upregulation of CANAR in response to sugars led us to hypothesize that CANAR may regulate sugar distribution. Notably, inducing *CANAR* overexpression in *XVE>>CANAR-3xHA* seedlings by growing them on 0.5x MS media with β-estradiol strongly reduced growth (Supplemental Figure 6H, J). This pleiotropic phenotype is reminiscent of various sugar transporter mutants or overexpression lines (Xue et al., 2022). This phenotype was partially rescued by external sucrose application (Supplemental Figure 6I, K). Therefore, we examined the expression of sugar transporters in plants overexpressing *CANAR*. SWEETs have been most extensively characterized in *Arabidopsis thaliana,* which contains four SWEET clades: I and II for final distribution of sucrose, glucose, and fructose within sink tissues, III for phloem loading and unloading, and IV for vacuolar sugar storage (Xue et al., 2022). Additionally, the Arabidopsis genome encodes nine SUC transporters (SUC1-9) (Bavnhøj et al., 2023). We selected *SWEET11*/*12*, which are expressed in leaf phloem parenchyma cells and affect vascular development (Le Hir et al., 2015), and *SWEET16/17*, which function in root vacuolar storage of glucose and fructose (Guo et al., 2014). For the *SUCs*, we chose *SUC1/2/3/4*, which are expressed in the shoot and root, with SUC2 being the main contributor to shoot-to-root sucrose transport (Durand et al., 2018). We induced *CANAR* expression overnight to allow for sufficient protein translation while avoiding secondary effects from prolonged treatment. All tested *SWEETs*, except *SWEET12*, were strongly downregulated (Supplemental Figure 6B). *SUC1* and *SUC2* were downregulated as well, while *SUC3* was

upregulated (Supplemental Figure 6C). In a complementary experiment, we tested *SWEETs* and *SUCs* expression in the *canar-3 irk-4* double mutant. We found that *SWEET11* and *SWEET16* were downregulated, and *SUC1* was slightly upregulated (Supplemental Figure 6D, E). Except for a modest change in *SUC2*, we did not observe any pronounced effect in the *canar-3* single mutant (Supplemental Figure 6F, G), which aligns with its reported redundancy with IRK (Goff et al., 2023). Moreover, tissue-specific effects may be concealed due to the inherently low resolution of RT-qPCR using whole seedlings.

These results indicate that sugar transporters are downstream of the CARMA-CANAR module activity. We utilized a widely used phloem-mobile probe 5-carboxyfluorescein diacetate (CFDA) to substantiate our hypothesis further. When applied to leaves, CFDA is cleaved by endogenous esterases to produce fluorescent dye. The dye is transported to sink tissues where it can be visualized (Ross-Elliott et al., 2017). We applied CFDA to leaves of Col-0, *canar-3*, *canar-3 irk-4*, and *XVE>>CANAR-3xHA*, and after 45 min, we analyzed CFDA accumulation in root meristem using confocal microscopy. We saw an increased accumulation of CFDA in *canar-3 irk-4* compared to Col-0, suggesting a higher content of osmotically active sugars in the root meristem. Conversely, the majority of *XVE>>CANAR-3xHA* roots after induction did not exhibit any staining (Figure 5A, B), evidencing a lower content of sugars. No reproducible differences were observed for *canar-3*, *carma-1*, or *XVE>>CARMA* lines (Figure 5A, B and Supplemental Figure 7A, B), which is most likely due to their weaker stele area phenotype, in contrast to *canar-3 irk-4* and *XVE>>CANAR-3xHA* (Goff et al., 2023), and low resolution of the CFDA approach.

The expected higher sugar content in the roots should be accompanied by a decrease in root osmotic potential, promoting water uptake into the roots and increasing turgor pressure. Conversely, lower sugar content reduces water uptake and decreases turgor pressure. As the assessment of turgor pressure is problematic and complicated for a number of reasons, we measured root osmotic potential as a proxy for estimating internal cell pressure. Consistent with our genetic and microscopic data, a more negative osmotic potential was found in roots of the *canar-3 irk-4* double mutant compared to Col-0, whereas *XVE>>CANAR-3xHA* had a less negative osmotic potential after induction (Figure 5C, D). No difference was observed for the *canar-3* mutant, again likely reflecting its subtle phenotype. We hypothesize that the regulation of the content of osmotically active sugars in root cells governs the extent of water uptake, which affects their internal pressure and, thus, the observed changes in cell size.

Discussion

Here, we propose that the CARMA-CANAR module acts as a novel osmoregulatory system controlling cell size in the stele in response to external osmolality. Based on our genetics, molecular, microscopy, and biophysical data, we conclude that CANAR activity regulates the shoot-to-root phloem transport of sugars, which influences internal pressure via cellular water uptake and, thus, resultant cell size (Figure 6). Root vascular cells in *XVE>>CARMA/canar-3* transgenic lines have a higher content of osmotically active sugars, causing increased water uptake

and larger cell size on hypotonic media. On hypertonic media, the higher sugar content is countered by the osmolality of the environment; hence, the cell size is not affected. In contrast, vascular cells in *carma-1/XVE>>CANAR* lines have a lower content of sugars, which leads to decreased water retention and, thus, smaller cell size on hypertonic media. This effect is absent in hypotonic media, where water can diffuse inside the cells to balance the osmolality difference.

CANAR is expressed both in xylem and protophloem and is upregulated by PM-permeable sugars in both domains. The *CARMA* fine-tunes *CANAR* expression predominantly in protophloem, likely via modulation of sensitivity to sugars. Since *CARMA* and *CANAR* expression response to sugar is similar (Figure 4D, E), it seems *CARMA* creates a feedback loop to establish a differential of CANAR expression between the xylem and protophloem. At this point, we are not certain why this differential is essential for cell adaptation to external osmolality.

The shoot-to-root transport of sugars consists of 3 steps: 1) phloem loading, 2) phloem movement, and 3) phloem unloading. Since we did not see any CFDA dye accumulation locked in root phloem in tested transgenic lines (Figure 5A, B), the CARMA-CANAR function in step 3 can be excluded. Water exchange between xylem and phloem generates hydrostatic pressure differences between source and sink, driving the flow of the phloem content (Knoblauch et al., 2016; Hardtke, 2023). Taking into account the strong expression of CANAR in xylem, the CARMA-CANAR involvement in step 2 is conceivable. In any case, the identification of downstream targets of CANAR is required to obtain further mechanistic insight.

A link between subcellular sugar distribution and internal cell pressure was proposed previously (McGaughey et al., 2016), where the SWEETs and aquaporins in *Setaria viridis* guide sucrose and water partitioning between vacuoles, cytosol, and the storage parenchyma apoplast to adjust cell turgor. Our results indicate that CANAR modifies the expression of *SUCs* and *SWEETs*, but it is unclear whether this is a causal effect or compensatory mechanism due to an intricate system of sugar distribution, highlighting the central role of sugars in plant growth and development. For perspective, the *SWEET* family in Arabidopsis contains 20 genes, whereas animal genomes have only one (Julius et al., 2017). Moreover, the exact molecular function of sugar transporters in phloem loading/unloading is not entirely clear. Considering the causal effect, direct interaction is unlikely, given that CANAR is a PM-localized pseudokinase and influences the expression of both PM- and vacuolar-localized sugar transporters. Thus, it is more plausible that CANAR controls the regulator/s of sugar transporters' expression.

Our hypothesis about the osmoregulatory function of the CARMA-CANAR module may explain the extra endodermal divisions in the *irk-4* and *canar-3 irk-4* mutants and their absence in *canar-3* (Campos et al., 2020; Goff et al., 2023). Larger cells in the stele generate elevated mechanical pressure on the endodermis, the pressure-buffering tissue of the root (Hamant and Haswell, 2017). Both *canar-3* and *irk-4* plants have an enlarged stele area, although the increase is greater in *irk-4*. This suggests there is a certain pressure threshold after extra divisions in the

endodermis are induced as a coping mechanism to dissipate the built-up mechanical pressure in the stele. This hypothesis is corroborated by the *canar-3 irk-4* double mutant, in which the stele area was more enlarged than in the single mutants, resulting in a higher incidence of extra endodermal divisions compared to *irk-4* (Goff et al., 2023). In line with our hypothesis, a cellulose-deficient *korrigan-1* mutant displayed root thickness twice that of the wild type (Mielke et al., 2021). The enlargement resulted mostly from cortex cells. Swollen cortex cells generated mechanical pressure towards the outer epidermal cells and cells of inner tissues. Still, mechanical stress, as evidenced by elevated jasmonate signaling, was observed only in endodermal and pericycle cells. The authors reasoned that epidermal cells dissipated the excessive pressure by expanding outward into the rhizosphere, and therefore, no extra cell divisions were induced in the endodermis.

The observations that *IRK* mutant (Campos et al., 2020), *CARMA* (Figure 2A-D) and *CANAR* (Hajný et al., 2020) mutant/overexpressing lines exhibit defects in leaf vascular patterning suggest that stele area and leaf vein patterning (mediated via auxin canalization) are likely developmentally co-dependent. It is possible that an appropriate stele area is required for undisturbed vascular patterning or that sugars are vital signaling molecules instructing auxin canalization and, thus, vasculature establishment. However, we cannot uncouple these two phenomena as the vasculature in cotyledons is already established in the embryo. Both scenarios are plausible as mechanical signals (laser ablation) in the shoot meristem induce reorientation of PIN1 auxin exporter (Heisler et al., 2010), and leaf vasculature still forms, although imperfectly when auxin directional transport is not functional (Verna et al., 2019). Perhaps the residual vein-patterning activity could be attributed to positional information determined by the sugar transport? Alternatively, SWEET transporters might transport auxin, as it was recently reported that *Arabidopsis* SWEET13/14 proteins can transport multiple forms of gibberellins (Kanno et al., 2016). This broad substrate specificity is also displayed by ABCB transporters, which contribute to directional auxin transport (Cho and Cho, 2013).

Besides the energy value of sugars, they also serve as signaling molecules. An extensive sugar-auxin signaling interaction network was recently described (Mishra et al., 2022). For instance, high glucose levels increased PIN2-GFP accumulation at the PM, promoting basipetal auxin transport in *Arabidopsis* (Mishra et al., 2009) while compromising PIN1-GFP expression, reducing auxin concentration in the root tip (Yuan et al., 2014). Moreover, external sugar (glucose/sucrose) application facilitated the accumulation of auxin on the concave side of the apical hook and contributed to the maintenance of the apical hook in a closed state (Chen et al., 2024). Given the interaction of CANAR with PIN1 (Hajný et al., 2020), the CARMA-CANAR module could be involved in the intricate interplay between sugar and auxin.

Manipulation of sugar distribution in plants is an obvious strategy for agriculture. Increasing the sugar content in roots can, besides improving the nutritional value, also change plant susceptibility to drought, cold, and heat stress (Julius et al., 2017). However, progress is hindered

by a lack of known molecular regulators of sugar transporters. To our knowledge, CANAR is the first receptor controlling sink-to-source sugar transport. Our work may provide key entry points into the understanding of the intricate regulation of sugar distribution.

Material and Methods

Plant Materials and Growth Conditions

All *Arabidopsis thaliana* lines were in Columbia-0 (Col-0) background. The T-DNA insertional mutant of *carma-1* (SAIL_704_A04) was obtained from NASC and genotyped with the primers listed in Supplemental Table 2. The *canar-3* (*pxc2-3*, SM_3_31635), *canar-3/pxc2-3 irk-4*, and *XVE>>CANAR-3xHA* were described previously (Goff et al., 2023). Transgenic line *canar-3xXVE>>CARMA* was generated by crossing. Seeds were sterilized with 70% ethanol for 5 min and then with 100% ethanol for another 5 min. Seeds were plated on 1% plant agar pH 5.9 (Duchefa) supplemented with 0.5x Murashige and Skoog (0.5x MS) media basal salts (Duchefa) without sugar unless otherwise indicated. 5-days old seedlings were used for imaging (counting 5 days after placement in the Phytochamber) Transgenic lines with the β-estradiol inducible promoter (*XVE*) were grown on 5 μM β-estradiol from germination unless otherwise indicated. Plates were sealed with 3M micropore tape. Seeds were stratified on plates at 4˚C for 1-2 days before being placed in a Phytochamber (16h light/8h dark cycle at a constant temperature of 21˚C, light intensity ~ 700-foot candle).

Cloning and Plant Transformation

Transcriptional reporter for *CANAR* (AT5G01890) was constructed by LR recombination of 4.7 kb promoter in pENTR5'-TOPO (Goff et al., 2023) with NLS-GFP-GUS and 285 bp of *CANAR* 3'UTR region (*ter*) in pENTR2B (generated via Gibson assembly-NEBuilder Hifi DNA assembly Master Mix) into pK7m24GW-FAST destination vector. The deletion of 157 bp of *CARMA* (until annotated 5' UTR of *CANAR*) was performed by amplifying truncated *pCANAR* in pENTR5'-TOPO with primers containing a SalI restriction site. The amplicon was cut with SalI for 30 min (FastDigest; Thermo), cleaned, and ligated overnight at 16˚C (T4 DNA ligase; NEB). The same approach was used for the second deletion (353 bp) of the *CARMA* locus. All three versions: *pCANAR::NLS-GFP-GUS-ter*, *pCANAR_CARMAΔ::NLS-GFP-GUS-ter* and *pCANAR_CARMAΔΔ::NLS-GFP-GUS-ter* were transformed into *carma-1* (SAIL_704_A04). Transcriptional reporters for *CARMA* (AT5G00810) were constructed by inserting 1300 bp *CARMA* promoter into pDONRP4-P1R via BP reaction and inserting 4975 bp *CARMA* promoter into pENTR5'TOPO via Gibson assembly. pDONRP4-P1R was recombined into pMK7S*NFm14GW, and pENTR5'TOPO with NLS-GFP-GUS in pENTR2B (NLS-GFP-GUS fragment was amplified from pMK7S*NFm14GW and inserted in pENTR2B via SalI restriction and subsequent ligation) into pH7m24GW destination vector via LR reaction. Translation reporters were constructed using Invitrogen Multisite Gateway technology. *pCANAR* (in pENTR

5' TOPO), *pCVP2-XVE* (in pDONRP4-P1R) were recombined with *CANAR* (genomic fragment without stop codon in pENTR-D-TOPO) (Goff et al., 2023) and with *GFP-ter* (GFP flanked by pkpapkpa linker at N-terminus and *CANAR* 285 bp 3' UTR region at C-terminus in pDONRP2r-P3) via LR reaction. For a generation of *XVE>>CARMA*, the genomic fragment of *CARMA* (AT5G00810) was amplified from Col-0 genomic DNA and recombined into the pDONRP221 entry vector via BP reaction. This was then recombined into the pMDC7 destination vector via LR reaction. All primers used are listed in Supplemental Table 2.

Plant transformation

Transgenic *Arabidopsis thaliana* plants were generated by the floral dip method using *Agrobacterium tumefaciens* (strain GV3101). Ecotype Columbia-0 (Col-0) served as the wild-type background for all lines.

CRISPR-Cas9

The transfer DNA (T-DNA) construct was constructed by cloning the two Cas9 spacer sequences "TGGCATGGACATGGTTAATG" and "GTTGGATTCCTCCAAGGTCT" as annealed oligonucleotides into the Gateway-compatible vectors pEn-Sa-Chimera and pDe-Sa-Cas9 EC, which carries *Staphylococcus aureus* Cas9 under the control of an egg cell-specific promoter, as described previously (Rönspies et al., 2022a). *A. thaliana* Columbia seeds were stratified overnight at 4 °C and cultivated in the greenhouse under 16h light/8h dark conditions at 22 °C on soil (1:1 mixture of Floraton 3 (Floragard) and vermiculite (2–3mm, Deutsche Vermiculite Dämmstoff)). After 4-5-weeks of growth, the plants were transformed with the CRISPR/Cas construct via Agrobacterium-mediated floral dip transformation. The transformed plants were cultivated for another 4-5 weeks until seed set. T1 seeds were surface-sterilized with 4% sodium hypochlorite and stratified overnight at 4 °C. The stratified seeds were sown on germination medium (4.9 g l^{-1} Murashige and Skoog medium, 10 g l^{-1} saccharose, pH 5.7 and 7.6 g l^{-1} plant agar) with phosphinotricin and cefotaxime in sterile culture. The plates were placed in a growth chamber at 22 °C under 16h light/8h dark conditions for 2 weeks. T1 primary transformants were selected and then cultivated in the greenhouse for 6-7 weeks until seed set. The T2 seeds were stratified and sown on germination medium without additives for 2 weeks. Afterwards, the plants were screened for the presence of the deletion via PCR by combining the primers oMR765 "GAGATGAAGTTGTTTCAGGGAGAC" and oMR766 "GGAGTCAAATATGGGCCTGATATTC", spanning the deletion site, via bulk and individual plant screenings. For bulk screenings, one leaf each from 40 plants was cut off and the leaves combined in one 1.5 ml reaction tube. For individual plant screenings, one leaf per plant was cut off and placed into separate 1.5 ml reaction tubes. The DNA extraction and screening was carried out as described previously (Rönspies et al., 2022b). The presence of the deletions was confirmed by sequencing of the junctions by Eurofins Genomics. The software ApE (v2.0.55) was used for alignment and analysis of the sequencing data. Out of 200 screened plants, three tested positive for the deletion. Two of these lines (*canar-4 C2* and *C4*) were chosen for propagation and further

analyses. The T3 offspring of these two lines were subjected to individual DNA extraction and screening to identify the individual plants harboring the deletion in the homozygous state. The plants were genotyped by PCR using primers specific for the deletion (oMR765/oMR766) as well as for the two wildtype (WT) junctions spanning the Cas9 cut sites (WT junction 1: oMR765/oMR792: GATTCTTGATCTCTCCGCCAAC; WT junction 2: oMR793: TATGTAATGTTAAATCCCTGTGCACC/oMR766). Homozygous plants were propagated in the greenhouse, and the seeds were harvested after 6-7 weeks.

RNA extraction, cDNA synthesis, and quantitative RT-PCR analysis

Total RNA was isolated from seedlings for gene expression analysis in mutants and overexpressing lines or from roots for RNA sequencing using Spectrum Plant Total R.N.A. Kit (Sigma). RNA was treated with TURBO DNAse (Thermo) to avoid genomic DNA contamination. Three independent biological replicates were done per sample. For cDNA synthesis (RevertAid First Strand cDNA Synthesis kit, Thermo), 2 µg of total RNA was used with Random Hexamer Primers mix (for RT-PCR of *CARMA* in Fig.1D) or with Oligo(dT) for the rest of the RT-qPCRs. The generated cDNA was analyzed on the StepOnePlus Real-Time PCR system (Life Technologies) with gb SG PCR Master Mix (Generi Biotech) according to the manufacturer's instructions. The relative expression was normalized to *SERINE/THREONINE PROTEIN PHOSPHATASE, PP2A (AT1G69960)*. Three technical replicates were performed. All primers used are listed in Supplemental Table 2.

Confocal microscopy

Five-day-old roots were stained with propidium iodide (PI) (10 µg/mL) and visualized via laser scanning confocal microscopy using a Zeiss LSM900 with a 40x water immersion objective. Fluorescent signals were visualized as PI (excitation 536 nm, emission 585-660 nm) and eGFP (excitation 488 nm, emission 492-530 nm). For stele area analysis, Z-stacks of approximately 100 µm were taken. ImageJ software was used for image postprocessing and quantification of stele area.

Histological analyses

β-glucuronidase (GUS) staining was performed as described in (Prát et al., 2018). The staining reaction was stopped with 70% ethanol and left for two days to remove chlorophyll. Seedlings were mounted in chloral hydrate and examined using a stereomicroscope (Olympus). ClearSee tissue clearing (Kurihara et al., 2015) was performed to count the cells in the transverse optical sections. The seedlings were fixed in 4% PFA in PBS (1h in vacuum), washed with PBS, and placed into ClearSee solution (25% urea, 15% sodium deoxylate, and 10% xylitol) for at least 3 days. Then, the seedlings were transferred into 0.1% Calcofluor White in ClearSee solution for 60 min, followed by a wash with ClearSee solution for 30 min; then mounted on slides with ClearSee. Two-sided tape was used on slides to prevent tissue disruption.

Stele area and vascular cell number quantification

Z-stacks of ~100 μm (1μm thick slices) capturing the root meristematic zone were acquired. The bleach correction plugin in ImageJ was applied to all images to compensate for decreasing PI signal in the deeper part of the root. The stele area and the number of vascular cells were assessed in the transverse sections located ~100 μm above QC using ImageJ.

Quantification of *pCANAR* expression in protophloem

Z-stacks of approximately 100 μm capturing the root meristematic zone was acquired. Multiple transverse sections with nuclear GFP fluorescence in xylem and protophloem in the same plane were taken for each Z-stack. The fluorescent signal in the protophloem was normalized to the xylem signal in each transverse section, and the average value of all sections from one root was calculated and plotted into a graph.

Software

Postprocessing of confocal images was done in ImageJ (https://imagej.nih.gov/ij/). Figures were generated in Adobe Illustrator or Biorender. Graphs and statistics were completed in GraphPad Prism9.

5 'and 3 'RACE experiments

The 5'RACE-seq library was generated from five-day-old roots with template-switching RT following the protocol outlined in (Montez et al, 2023). Shortly, 500 ng of total RNA, post DNAse treatment, served as the template for cDNA generation using SuperScript II. The resulting cDNA was purified using AMPure XP magnetic beads (Beckman Coulter) and amplified in series of three PCR reactions with specific primers (1^{st} PCR: only TSO_n1, 2^{nd} PCR: TSO_n2 and CARMA_5RACE, 3^{rd} PCR: Illumina indexing primers) and Phusion polymerase. Following quality checks, the final PCR product was sequenced using Illumina MiSeq.

The 3'RACE-seq was completed based on the procedure described by Warkocki et al (2018) with ligation of the pre-adenylated adaptor to the 3'end of the RNA using truncated T4 RNA Ligase 2. RNA ligated with RA3_15N adaptor (containing UMI) was cleaned on AMPure XP magnetic beads and subjected to RT reaction with SuperScrit III. After three rounds of PCR with specific primers (1^{st}PCR: CARMA_3RACE and RTPXT, 2^{nd}PCR: mXTf and mXTr, 3^{rd} PCR: Illumina indexing primers) and cleaning each PCR reaction on AMPure beads, prepared libraries were sequenced using Illumina MiSeq.

Sequence reads were trimmed to remove adapter sequences using cutadapt (v1.18; Martin, 2011). STAR (v2.7.8a; Dobin et al, 2013) was utilized to align the reads to the reference genome, followed by UMI-based filtering using UMI-tools (v1.1.0; Smith et al, 2017). The position of the reads ends nucleotide was extracted using bedtools (v2.30.0; Quinlan & Hall, 2010). All primers used are listed in Supplemental Table 2.

CFDA staining

5-carboxyfluorescein diacetate (Sigma-Aldrich, CAS: 79955-27-4) was diluted in DMSO to create 10 mM stock. Shoots of 5-day-old seedlings were placed on a glass cover lid, and 2 μL of working 1 mM solution in water was placed on one leaf. After 45 min, the seedlings were placed into a chamber with an agar block stained with propidium iodide and imaged using confocal microscopy in a GFP channel (excitation 488 nm, emission 492-530 nm).

Root osmotic potential

Root osmotic potential (ψs) was measured using C-52 thermocouple psychrometric chambers and an HR-33T Dew Point Microvoltmeter (Wescor, USA) in dew point mode (Campbell et al., 1973; Briscoe, 1986). Prior to ψs measurement, root samples were subjected to a freeze-thaw cycle and equilibrated for 40 min after insertion into the chamber. Each sample consisted of roots from 5 seedlings. The chambers were calibrated with NaCl solutions of different osmolality.

Osmolality measurement

Osmometer 3320 (Advanced Instruments) was used for measuring liquid media osmolality according to the manufacturer's instructions. The machine was calibrated using calibration standards at 50 mOSm/kg, 850 mOSM/kg and 2000 mOsm/kg. A sampler tip was inserted into the sampler and 20 μL of sample was loaded. The sample was visually inspected to avoid any bubbles, and any excess solution on the sampler tip was removed using soft, no-lint, non-ionic paper tissue. The osmometer chamber was cleaned, and the sample was inserted to measure osmolality values. All tested liquid media were mixed for 30 minutes on a magnetic stirrer to ensure complete dissolution of all substances. The media were measured at room temperature.

Author contributions

Conceptualization: JH; Funding: JH, ON; Writing, editing and interpretation of data: JH, SS, SSw, AP, JMVN, DZ, CH, RMIKR; Methodology: JH, DZ, SS, TT, RMIKR; RACE experiments: SS, SSw; Bioinformatics: MK, Microscopy: JH, RMIKR; Cloning: JH, DZ, TT; Generation of transgenic lines: JH, TT; CRISPR/Cas9: MMR., HP, Psychrometry: MŠ

Acknowledgements

We acknowledge the EMBO long-term fellowship (ALTF 217-2021) and Junior grant UPOL (JG_2024_003) for supporting JH. The work of RMIKR and JMVN is supported by NSF CAREER award #1751385.

Declarations

The authors declare no conflict of interest.

References

588 Ali, O., Cheddadi, I., Landrein, B., and Long, Y. (2023). Revisiting the relationship between
589 turgor pressure and plant cell growth. *New Phytol.* 238:62–69.

590 Bavnhøj, L., Driller, J. H., Zuzic, L., Stange, A. D., Schiøtt, B., and Pedersen, B. P. (2023).
591 Structure and sucrose binding mechanism of the plant SUC1 sucrose transporter. *Nat.*
592 *Plants* 9:938–950.

593 Briscoe, R. (1986). Thermocouple Psychrometers for Water Potential Measurements. In
594 *Advanced Agricultural Instrumentation: Design and Use* (ed. Gensler, W. G.), pp. 193–
595 209. Dordrecht: Springer Netherlands.

596 Campbell, E. C., Campbell, G. S., and Barlow, W. K. (1973). A dewpoint hygrometer for water
597 potential measurement. *Agric. Meteorol.* 12:113–121.

598 Campos, R., Goff, J., Rodriguez-Furlan, C., and Van Norman, J. M. (2020). The Arabidopsis
599 Receptor Kinase IRK Is Polarized and Represses Specific Cell Divisions in Roots. *Dev.*
600 *Cell* 52:183-195.e4.

601 Chen, J., Yang, L., Zhang, H., Ruan, J., and Wang, Y. (2024). Role of sugars in the apical hook
602 development of Arabidopsis etiolated seedlings. *Plant Cell Rep.* 43:131.

603 Cho, M., and Cho, H. (2013). The function of ABCB transporters in auxin transport. *Plant*
604 *Signal. Behav.* 8:e22990.

605 Chorostecki, U., Bologna, N. G., and Ariel, F. (2023). The plant noncoding transcriptome: a
606 versatile environmental sensor. *EMBO J.* 42:e114400.

607 Cosgrove, D. J. (2016). Plant cell wall extensibility: connecting plant cell growth with cell wall
608 structure, mechanics, and the action of wall-modifying enzymes. *J. Exp. Bot.* 67:463–
609 476.

610 Durand, M., Mainson, D., Porcheron, B., Maurousset, L., Lemoine, R., and Pourtau, N. (2018).
611 Carbon source–sink relationship in Arabidopsis thaliana: the role of sucrose transporters.
612 *Planta* 247:587–611.

613 Fandino, A. C. A., Jelinkova, A., Marhava, P., Petrasek, J., and Hardtke, C. S. (2023). Ectopic
614 assembly of an auxin efflux control machinery shifts developmental trajectories Advance
615 Access published September 17, 2023, doi:10.1101/2023.09.16.558043.

616 Fukuda, H., and Ohashi-Ito, K. (2019). Vascular tissue development in plants. *Curr. Top. Dev.*
617 *Biol.* 131:141–160.

618 Geiger, D. (2020). Plant glucose transporter structure and function. *Pflüg. Arch. - Eur. J. Physiol.*
619 472:1111–1128.

620 Goff, J., Rony, R. M. I. K., Ge, Z., Hajný, J., Rodriguez-Furlan, C., Friml, J., and Norman, J. M.
621 V. (2023). PXC2, a polarized receptor kinase, functions to repress ground tissue cell

622 divisions and restrict stele size Advance Access published March 19, 2023,
623 doi:10.1101/2021.02.11.429611.

624 Guo, W.-J., Nagy, R., Chen, H.-Y., Pfrunder, S., Yu, Y.-C., Santelia, D., Frommer, W. B., and
625 Martinoia, E. (2014). SWEET17, a Facilitative Transporter, Mediates Fructose Transport
626 across the Tonoplast of Arabidopsis Roots and Leaves. *Plant Physiol.* 164:777–789.

627 Hajný, J., Prát, T., Rydza, N., Rodriguez, L., Tan, S., Verstraeten, I., Domjan, D., Mazur, E.,
628 Smakowska-Luzan, E., Smet, W., et al. (2020). Receptor kinase module targets PIN-
629 dependent auxin transport during canalization. *Science* 370:550–557.

630 Hamant, O., and Haswell, E. S. (2017). Life behind the wall: sensing mechanical cues in plants.
631 *BMC Biol.* 15:59.

632 Hardtke, C. S. (2023). Phloem development. *New Phytol.* 239:852–867.

633 Heisler, M. G., Hamant, O., Krupinski, P., Uyttewaal, M., Ohno, C., Jönsson, H., Traas, J., and
634 Meyerowitz, E. M. (2010). Alignment between PIN1 Polarity and Microtubule
635 Orientation in the Shoot Apical Meristem Reveals a Tight Coupling between
636 Morphogenesis and Auxin Transport. *PLOS Biol.* 8:e1000516.

637 Hohl, M., and Schopfer, P. (1991). Water Relations of Growing Maize Coleoptiles 1. *Plant*
638 *Physiol.* 95:716–722.

639 Julius, B. T., Leach, K. A., Tran, T. M., Mertz, R. A., and Braun, D. M. (2017). Sugar
640 Transporters in Plants: New Insights and Discoveries. *Plant Cell Physiol.* 58:1442–1460.

641 Kanno, Y., Oikawa, T., Chiba, Y., Ishimaru, Y., Shimizu, T., Sano, N., Koshiba, T., Kamiya, Y.,
642 Ueda, M., and Seo, M. (2016). AtSWEET13 and AtSWEET14 regulate gibberellin-
643 mediated physiological processes. *Nat. Commun.* 7:13245.

644 Knoblauch, M., Knoblauch, J., Mullendore, D. L., Savage, J. A., Babst, B. A., Beecher, S. D.,
645 Dodgen, A. C., Jensen, K. H., and Holbrook, N. M. (2016). Testing the Münch
646 hypothesis of long distance phloem transport in plants. *eLife* 5:e15341.

647 Kurihara, D., Mizuta, Y., Sato, Y., and Higashiyama, T. (2015). ClearSee: a rapid optical
648 clearing reagent for whole-plant fluorescence imaging. *Development* 142:4168–4179.

649 Le Hir, R., Spinner, L., Klemens, P. A. W., Chakraborti, D., de Marco, F., Vilaine, F., Wolff, N.,
650 Lemoine, R., Porcheron, B., Géry, C., et al. (2015). Disruption of the Sugar Transporters
651 AtSWEET11 and AtSWEET12 Affects Vascular Development and Freezing Tolerance in
652 Arabidopsis. *Mol. Plant* 8:1687–1690.

653 McGaughey, S. A., Osborn, H. L., Chen, L., Pegler, J. L., Tyerman, S. D., Furbank, R. T., Byrt,
654 C. S., and Grof, C. P. L. (2016). Roles of Aquaporins in Setaria viridis Stem
655 Development and Sugar Storage. *Front. Plant Sci.* 7.

Mielke, S., Zimmer, M., Meena, M. K., Dreos, R., Stellmach, H., Hause, B., Voiniciuc, C., and Gasperini, D. (2021). Jasmonate biosynthesis arising from altered cell walls is prompted by turgor-driven mechanical compression. *Sci. Adv.* 7:eabf0356.

Mishra, B. S., Singh, M., Aggrawal, P., and Laxmi, A. (2009). Glucose and Auxin Signaling Interaction in Controlling Arabidopsis thaliana Seedlings Root Growth and Development. *PLOS ONE* 4:e4502.

Mishra, B. S., Sharma, M., and Laxmi, A. (2022). Role of sugar and auxin crosstalk in plant growth and development. *Physiol. Plant.* 174:e13546.

Prát, T., Hajný, J., Grunewald, W., Vasileva, M., Molnár, G., Tejos, R., Schmid, M., Sauer, M., and Friml, J. (2018). WRKY23 is a component of the transcriptional network mediating auxin feedback on PIN polarity. *PLOS Genet.* 14:e1007177.

Rönspies, M., Schindele, P., Wetzel, R., and Puchta, H. (2022a). CRISPR–Cas9-mediated chromosome engineering in Arabidopsis thaliana. *Nat. Protoc.* 17:1332–1358.

Rönspies, M., Schindele, P., Wetzel, R., and Puchta, H. (2022b). CRISPR–Cas9-mediated chromosome engineering in Arabidopsis thaliana. *Nat. Protoc.* 17:1332–1358.

Ross-Elliott, T. J., Jensen, K. H., Haaning, K. S., Wager, B. M., Knoblauch, J., Howell, A. H., Mullendore, D. L., Monteith, A. G., Paultre, D., Yan, D., et al. (2017). Phloem unloading in Arabidopsis roots is convective and regulated by the phloem-pole pericycle. *eLife* 6:e24125.

Scarpella, E., Marcos, D., Friml, J., and Berleth, T. (2006). Control of leaf vascular patterning by polar auxin transport. *Genes Dev.* 20:1015–1027.

Verna, C., Ravichandran, S. J., Sawchuk, M. G., Linh, N. M., and Scarpella, E. (2019). Coordination of tissue cell polarity by auxin transport and signaling. *eLife* 8:e51061.

Wang, K. C., and Chang, H. Y. (2011). Molecular Mechanisms of Long Noncoding RNAs. *Mol. Cell* 43:904–914.

Wang, J., Kucukoglu, M., Zhang, L., Chen, P., Decker, D., Nilsson, O., Jones, B., Sandberg, G., and Zheng, B. (2013). The Arabidopsis LRR-RLK, PXC1, is a regulator of secondary wall formation correlated with the TDIF-PXY/TDR-WOX4 signaling pathway. *BMC Plant Biol.* 13:94.

Xue, X., Wang, J., Shukla, D., Cheung, L. S., and Chen, L.-Q. (2022). When SWEETs Turn Tweens: Updates and Perspectives. *Annu. Rev. Plant Biol.* 73:379–403.

Yuan, T.-T., Xu, H.-H., Zhang, K.-X., Guo, T.-T., and Lu, Y.-T. (2014). Glucose inhibits root meristem growth via ABA INSENSITIVE 5, which represses PIN1 accumulation and auxin activity in Arabidopsis. *Plant Cell Environ.* 37:1338–1350.

690 Zuo, J., Niu, Q.-W., and Chua, N.-H. (2000). An estrogen receptor-based transactivator XVE
691 mediates highly inducible gene expression in transgenic plants. *Plant J.* 24:265–273.

692

693 **Figure legends**

694 **Fig. 1 *CARMA* has a complementary expression with *CANAR* in root protophloem**

695 (A) Confocal images of a primary root stained with propidium iodide (grey) expressing
696 *pCANAR::NLS-GFP-GUS-ter* (schematic depicted above images), shows *pCANAR* activity in
697 xylem (X), developing protophloem sieve elements (PPh), lateral root cap (LRC), and with weaker
698 expression in metaphloem precursors (MPh). (B) *pCANAR* activity in roots (left) and cotyledons
699 and true leaves (right, inset) visualized by β-glucuronidase (GUS) staining (blue). (C) A graphical
700 representation of the *CARMA-CANAR* genomic locus. (D) sqRT-PCR of *CARMA* RNA from 5-
701 day-old seedlings. (E) Confocal images of a primary root stained with propidium iodide (grey)
702 expressing *pCARMA(5kb)::NLS-GFP-GUS* (depicted above images), showing *pCARMA* activity
703 predominantly in PPh with weaker activity in MPh and X. (F) *pCARMA* activity in roots (left) and
704 cotyledons and true leaves visualized by β-glucuronidase (GUS) staining (blue). Numbers in
705 medial longitudinal confocal images represent the position of the transverse optical section taken
706 from a Z-stack. For each reporter, ≥10 roots were examined. Scale bars 20 μm. Other cell types:
707 Epi-epidermis, Co-cortex, En-endodermis, LRC-lateral root cap. See also Supplemental Figure 1.

708 **Fig. 2 *CARMA* regulates leaf vascular patterning and root stele area**

709 (A) and (C) representative images of cotyledon vasculature from 10-day-old Col-0, two
710 independent *35S::CARMA* transgenic lines, and *carma-1* seedlings. Scale bars, 100 μm. (B) and
711 (D) quantification of observed vein pattern phenotypes as a percentage. Black asterisks mark a
712 number of closed loops. Black arrowheads highlight extra branches. For each genotype, ≥66
713 cotyledons were analyzed. A Student's t-test compared the overall incidence of tested defects in
714 marked datasets (*P<0.05) (E) Transverse optical sections of 5-day-old root meristems stained
715 with propidium iodide (black) from two independent inducible CARMA overexpression
716 (*XVE>>CARMA*) lines (#1 and #8) on 0.2x MS medium with 5 μM (EST^+) and without (Mock)
717 β-estradiol. (F) Transverseal optical sections of 5-day-old root meristems stained with propidium
718 iodide of Col-0 and *carma-1* mutant on 1x MS. Green line indicates the measured stele area for
719 (G) and (H). (G) and (H) box plots showing stele area quantification of *XVE>>CARMA* and
720 *carma-1* on different concentrations of MS medium. Whiskers indicate max/min, box shows the
721 interquartile range with a black line showing the median. Colored symbols are measurements from
722 individual roots. The experiments were carried out three times (8-10 roots for each genotype per
723 replicate); one representative biological replicate is shown. A one-way ANOVA test compared
724 marked datasets (*P<0.05 and ****P<0.0001). Scale bars, 20 μm. Cell types: Epi-epidermis, Co-
725 cortex, En-endodermis, X-xylem, LRC-lateral root cap. The transverse optical sections were taken
726 approximately 100 μm from QC (quiescent center). See also Supplemental Figure 2 and 3.

Fig. 3 *CARMA* fine-tunes protophloem-specific expression of *CANAR*

(A) Representative confocal images of primary roots stained with propidium iodide (white) of *carma-1* plants expressing *pCANAR::NLS-GFP-GUS-ter, pCANAR_CARMAΔ::NLS-GFP-GUS-ter*, or *pCANAR_CARMAΔΔ::NLS-GFP-GUS-ter* reporters (schematics shown above images). Numbers #30, #27, and #11 mark particular independent transgenic lines. Both partial and complete deletion of *CARMA* led to increased *pCANAR* activity in the PPh (highlighted with a green label and arrowhead). Numbers represent the position of a transverse optical section taken from Z-stacks. (B) Box plot showing relative fluorescence of reporters in (A) where the signal in the PPh is normalized to that in the X (see the Material and Method section for details). Whiskers indicate the max/min, the box shows the interquartile range, and the median is shown with a black line. Colored symbols show measurements for individual roots. (C) Transverse optical sections of 5-day-old root meristems stained with propidium iodide (magenta) from plants expressing *XVE>>CANARx3HA* and *pCVP2>>CANAR-GFP-ter* grown on 1x MS medium with (EST^+) and without (Mock) β-estradiol from the time of germination. The outer edge of the stele is indicated by the yellow line. (D) Box plot showing stele area quantification of the plants in (C). Whiskers indicate the max/min, the box shows an interquartile range, and the median is shown with a black line. Colored symbols are measurements from individual roots. These experiments were done three times (8-10 roots for each genotype per experiment); one representative biological replicate is shown. A one-way ANOVA test compared marked datasets (*P<0.05, **P<0.01, and ***P<0.001). Scale bars, 20 μm. Cell types: Epi-epidermis, Co-cortex, En-endodermis, PPh-developing protophloem sieve elements, X-xylem, and LRC-lateral root cap. See also Supplemental Figure 4.

Fig. 4 *CARMA* mediates the sugar responsiveness of CANAR

(A) Representative confocal images of primary roots grown on 0.5x MS medium stained with propidium iodide (magenta) expressing *pCANAR::CANAR-GFP-ter* #2 and treated 5h in liquid 0.5x MS medium with Mock, 30 mM sucrose, 90 mM sucrose, 30 mM glucose, 30 mM mannitol and 30 mM sucrose + 30mM mannitol. The dark, non-fluorescent structure in the xylem cells is the nucleus. (B) Representative confocal images of primary roots grown on 0.5x MS medium stained with propidium iodide (magenta) expressing *pCANAR::CANAR-GFP-ter 2*. After 5 days, shoots were placed on a glass cover lid, and droplets of liquid 0.5x MS medium containing Mock, 90 mM sucrose, or 90 mM glucose were applied to the shoots (C). After 5h, root meristems were imaged. For each treatment, ≥12 roots were analyzed, and the images were acquired using comparable settings. Scale bar, 20 μm. Cell types: Epi-epidermis, Co-cortex, En-endodermis, X-xylem, and LRC-lateral root cap. White numbers at the bottom right corner indicate a frequency of observed expression pattern. Relative expression by RT-qPCR of *CARMA* and *CANAR* after spraying with 90 mM sucrose on 0.5x MS in (D) leaves and (E) roots. Relative expression by RT-qPCR of *CANAR* in Col-0 and *carma-1* after spraying with 90 mM sucrose in 0.5x MS in (F) leaves and (G) roots. Relative expression by RT-qPCR of *CANAR* in *XVE>>CARMA* grown on Mock or EST^+ after spraying with 90 mM sucrose in 0.5x MS in (H) leaves and (I) roots. The

graphs represent three biological replicates. Error bars represent SE. A one-way ANOVA test compared marked datasets (*P<0.05, **P<0.01, ***P<0.001 and ****P<0.0001). See also Supplemental Figure 5 and 6.

Fig. 5 CANAR regulates the shoot-to-root phloem transport of osmotically active compounds

(A) Representative images of 5-day-old seedlings grown on 0.2x MS for Col-0, *canar-3* and *canar-3 irk-4*, and on 1x MS with (EST^+) or without β-estradiol (Mock) for *XVE>>CANAR-3xHA*. Shoots were placed on a glass cover lid, and a 2 μL droplet of 1 mM CFDA in water was placed on each shoot. After 45 min, the seedlings were placed on an agar block stained with propidium iodide (grey) and imaged. Scale bar, 20 μm (B) A quantification of (A) by measuring the fluorescence intensity of CFDA in roots. Each colored symbol represents one biological experiment where fluorescence intensity in approximately 20 roots grown on one agar plate was measured and averaged. The average values were normalized to respective control. The median is shown with a black line. Three biological replicates were done for each genotype/treatment. A Student's t-test compared marked datasets (*P<0.05 and **P<0.01). (C) A quantification of osmotic potential of (C) Col-0, *canar-*, and *canar-3 irk*-4 roots grown on 0.2x MS and (D) *XVE>>CANAR-3xHA* roots grown on 1x MS with (EST^+, 3 days induction) or without β-estradiol (Mock). The experiment was carried out four times. Five roots per biological replicate were used. The graphs show data from four biological replicates, and error bars represent SD. A one-way ANOVA test compared marked datasets (**P<0.01 and ***P<0.001). See also Supplemental Figure 7.

Fig. 6 Graphical illustration of the CARMA-CANAR action

(A) The CARMA-CANAR module regulates phloem transport from shoot to roots. The availability of osmotically active compounds (mainly sugars) in stele cells determines water content and, thus, resultant cell size via internal pressure build-up. On hypotonic media, root stele cells in *XVE>>CARMA/canar-3* transgenic lines have a higher content of osmotically active sugars, leading to increased water uptake and larger cell size. On hypertonic media, the higher sugar content of stele cells is countered by the osmolality of the environment; hence, the cell size is not affected. In contrast, stele cells in *carma-1/XVE>>CANAR* lines have a lower content of sugars, which leads to decreased water retention and, thus, smaller cell size on hypertonic media. This effect is absent in hypotonic media, where water can diffuse inside the cells to balance the osmolality difference.

Supplemental Fig. 1 Characterization of the *CARMA* transcript

(A) and (B) The full-length transcript of *CARMA* based on 5' and 3' RACE results. Representative confocal images of a primary root stained with propidium iodide (grey) of roots showing expression of (C) *pCARMA(5kb)::NLS-GFP-GUS* and (D) *pCARMA(1.3kb)::NLS-GFP-GUS*. (E) *pCARMA* activity visualized by β-glucuronidase (GUS) staining in a root expressing *pCARMA(1.3kb)::NLS-GFP-GUS*. A minimum of 10 roots were examined for each reporter. Scale

bars, 20 μm. Cell types: Epi-epidermis, Co-cortex, En-endodermis, PPh-developing protophloem sieve elements, MPh-metaphloem precursors, X-xylem, LRC-lateral root cap.

Supplemental Fig. 2 Enlarged stele area phenotype upon *CARMA* overexpression is due to larger cells.

(A) The position of T-DNA insertion in the *carma-1* mutant. Relative expression by RT-qPCR of *CARMA* in (B) *carma-1*, (D) *35S::CARMA*, and (E) *XVE>>CARMA*. (C) Relative expression by RT-qPCR of *CANAR* in *carma-1*. The graphs represent three biological replicates. Error bars represent SE. (F) Distance between endodermis and lateral root cap in *XVE>>CARMA* line as visualized in (H) by the orange bidirectional arrow. The experiment was carried out three times (each with 10 roots per sample per genotype), data shown are from a single biological replicate. (G) The number of cells in stele in *XVE>>CARMA* with and without β-estradiol induction from the time of germination with 15-20 roots analyzed per line per condition. (H) Representative transverse optical sections taken ~100 μm from QC (quiescent center), where cell number was quantified for (G). These analyses were performed three times with ≥18 roots per genotype per condition. Graphs show the data from 1 biological replicate. (J) Box plot showing a quantification of root meristem lengths from (I). Box plots showing quantification of stele area (μm) on 0.2x MS in (K) *canar-3xXVE>>CARMA*, (L) *canar3/canar-4 C2/canar-4 C4* and on 0.2x MS with 64 mM mannitol in (M) *canar-3*, (N) *XVE>>CARMA* and (O) Col-0. Whiskers indicate the max/min, box shows interquartile range, and the median is shown with a black line. These analyses were performed three times with 9-10 roots per genotype. Graphs show the data from 1 biological replicate. Colored symbols are measurements from individual roots. A one-way ANOVA test compared marked datasets (*P<0.05 and **P<0.01). Scale bars, 20 μm. Cell types: Epi-epidermis, Co-cortex, En-endodermis, X-xylem, LRC-lateral root cap. The transverse optical sections were taken approximately 100 μm from QC (quiescent center).

Supplemental Fig. 3 Reduced stele area phenotype in *carma-1* is due to smaller cells.

(A) Number of cells within the stele in *carma-1* mutants grown on 1x MS compared to Col-0. (B) Representative transverse sections taken approximately 100 μm from QC (quiescent center) where stele cells were counted for (A) with 15-20 roots analyzed. The experiment was done three times. Graph shows the data from 1 biological replicate. (C) Measurement of the distance between the endodermis and LRC in Col-0 and *carma-1* on 1x MS media. (D) Representative images of the median longitudinal sections of the Col-0 and *carma-1* root meristems stained with PI. (E) Measurement of meristem length in Col-0 and carma-1 on 1x MS medium. These analyses were carried out three times with ≥15 roots per genotype. Graphs show the data from 1 biological replicate. Scale bars, 20 μm. Cell types: Epi-epidermis, Co-cortex, En-endodermis, Per-pericycle, X-xylem. (F) Schematic overview of the induced deletion. Red triangles and dashed lines indicate the location of the CRISPR/Cas9-induced double-strand breaks (DSB 1 and DSB 2). (G) DNA sequence of the two wildtype junctions (WT J1 and WT J2), the expected

composition of the deletion junction (Exp. del. J) as well as the deletion junctions present in the two lines canar-4 C2 and C4. The first guide sequence is highlighted in cyan and the corresponding protospacer adjacent motif (PAM) sequence in pink. The second guide sequence is highlighted in green and the corresponding PAM sequence in orange. Red triangles indicate the location of the CRISPR/Cas9-induced double-strand breaks. The first two lines show the original WT conformation. The line in the center shows the expected nucleotide composition of the deletion junction. The last two lines show the deletion junction after induction of the deletion in canar-4 C2 and C4. Insertions and deletions of bases at the break site are defined by dashes/slashes and the respective number of inserted/deleted bases.

Supplemental Fig. 4 *CARMA* regulates the protophloem-specific expression of *CANAR*

(A) Representative confocal images of primary roots stained with propidium iodide (white) of a second independent transgenic line of each *pCANAR::NLS-GFP-GUS-ter*, *pCANAR_CARMAΔ::NLS-GFP-GUS-ter*, and *pCANAR_CARMAΔΔ::NLS-GFP-GUS-ter* in *carma-1* (schematics of each reporter above the images). Numbers #21, #21, and #25 mark particular independent transgenic lines. Both partial and complete deletion of *CARMA* show increased *pCANAR* activity in the PPh (highlighted with green text and arrowhead). Numbers represent the position of a transverse optical section taken from Z-stacks. (B) Box plot shows the quantification of fluorescent signal from (A), where signal from the PPh is normalized to that from the X (see the Material and Method section for details). Whiskers indicate the max/min with boxes showing interquartile range, and a black line shows the median. Colored symbols indicate measurements from individual roots. These experiments were done three times (8-10 roots for each genotype per experiment); one representative biological replicate is shown. (C) Relative expression by RT-qPCR of *CANAR* in two independent lines of *35::CARMA* (#4 and #14). The graph represents three biological replicates. Error bars represent SE. (D) and (E) Box plot showing stele area quantification of *XVE>>CANARx3HA* and *pCVP2>>CANAR-GFP-ter* transgenic lines grown on 0.2x and 0.5x MS medium with (EST^+) and without (Mock) β-estradiol from the time of germination. Whiskers indicate the max/min, the box shows an interquartile range, and the median is shown with a black line. Colored symbols are measurements from individual roots. These experiments were done three times (9-10 roots for each genotype per experiment); one representative biological replicate is shown. A one-way ANOVA test compared marked datasets (*P<0.05, **P<0.01 and ***P<0.001). Scale bar, 20 μm. Cell types: Epi-epidermis, Co-cortex, En-endodermis, PPh-developing protophloem sieve elements, X-xylem, LRC-lateral root cap.

Supplemental Fig. 5 CANAR is specifically upregulated by PM-permeable sugars

(A) Representative confocal images of primary roots of two independent *pCANAR::CANAR-GFP-ter* lines (*#2* and *#9*) grown on 0.5x MS with or without 30 mM sucrose. (B) Representative confocal images of primary roots of *pCANAR::CANAR-GFP-ter #9* grown on 0.5x MS medium and treated 5h in liquid 0.5x MS medium with Mock, 30 mM sucrose, 90 mM sucrose, 30 mM

glucose, 30 mM mannitol and 30 mM sucrose+30mM mannitol. The dark, non-fluorescent structure in the xylem cells is the nucleus. Representative confocal images of primary roots of *pCANAR::CANAR-GFP-ter #2* grown on 0.5x MS medium and treated 5h in (C) liquid 0.5x MS medium with Mock or 30 mM NaCl or in (D) 0.2x, 0.5x or 1x MS liquid medium. The roots were stained with propidium iodide (magenta). Scale bar, 20µm. White numbers in the bottom right corner indicate a frequency of observed expression pattern. RT-qPCR expression analysis of *CANAR* and *CARMA* in (E) leaves or (F) roots of 6-day-old seedlings after spraying of 0.5x MS liquid media supplemented with 90 mM mannitol for 1h. The graphs show data from three biological replicates, and error bars represent SE.

Supplemental Fig. 6 Sugar effect on *CARMA* expression

(A) Representative confocal images of primary roots of *pCARMA(5kb)::NLS-GFP-GUS* grown on 0.5x MS and treated 5h in liquid 0.5x MS medium with Mock, 30 mM sucrose, 90 mM sucrose, 30 mM glucose, 30 mM mannitol or 30 mM sucrose+30mM mannitol. The roots were stained with propidium iodide (grey). Scale bar, 20µm. White numbers in the bottom right corner indicate a frequency of observed expression pattern. Relative expression by RT-qPCR of *SWEET11/12/16/17* in (B) *XVE>>CANAR-3xHA* (Mock vs. EST^+, 16h induction), (D) *canar-3 irk-4* and (F) *canar-3*. Relative expression by RT-qPCR of *SUC1/2/3/4* in (C) *XVE>>CANAR-3xHA* (Mock vs. EST^+, 16h induction), (E) *canar-3 irk-4* and (G) *canar-3*. The graphs represent three biological replicates. Error bars represent SE. Representative image of 6-days-old *XVE>>CANAR-3xHA* seedlings grown on (H) 0.5x MS Mock vs. EST^+ and (I) 0.5x MS+30 mM (1%) sucrose Mock vs. EST^+. (J) and (K) box plots showing quantifications of root length in (H) and (I). Whiskers indicate the max/min, the box shows an interquartile range, and the median is shown with a black line. Colored symbols are measurements from individual roots. These experiments were done three times; one representative biological replicate is shown. A one-way ANOVA test compared marked datasets (*P<0.05, **P<0.01, ***P<0.001 and ****P<0.0001).

Supplemental Fig. 7 *CARMA* involvement in the shoot-to-root phloem transport

(A) Representative images of 5-day-old seedlings grown on 1x MS for Col-0 and *carma*-1 and 1x MS with (EST^+) or without β-estradiol (Mock) for *XVE>>CARMA*. Shoots were placed on a glass cover lid, and a 2 µL droplet of 1 mM CFDA in water was placed on each shoot. After 45 min, the seedlings were placed on an agar block stained with propidium iodide (grey) and imaged. (B) A quantification of (A) by measuring the fluorescence intensity of CFDA in roots. Each colored symbol represents one biological experiment where fluorescence intensity in approximately 20 roots grown on one agar plate was measured and averaged. The average values were normalized to respective control. The median is shown with a black line. Three biological replicates were done for each genotype/treatment. A Student's t-test compared marked datasets.

Supplemental Tab. 1 Measured osmolality of experimental solutions

916 **Supplemental Tab. 2 Primers used in this study**

917

918

Fig.1

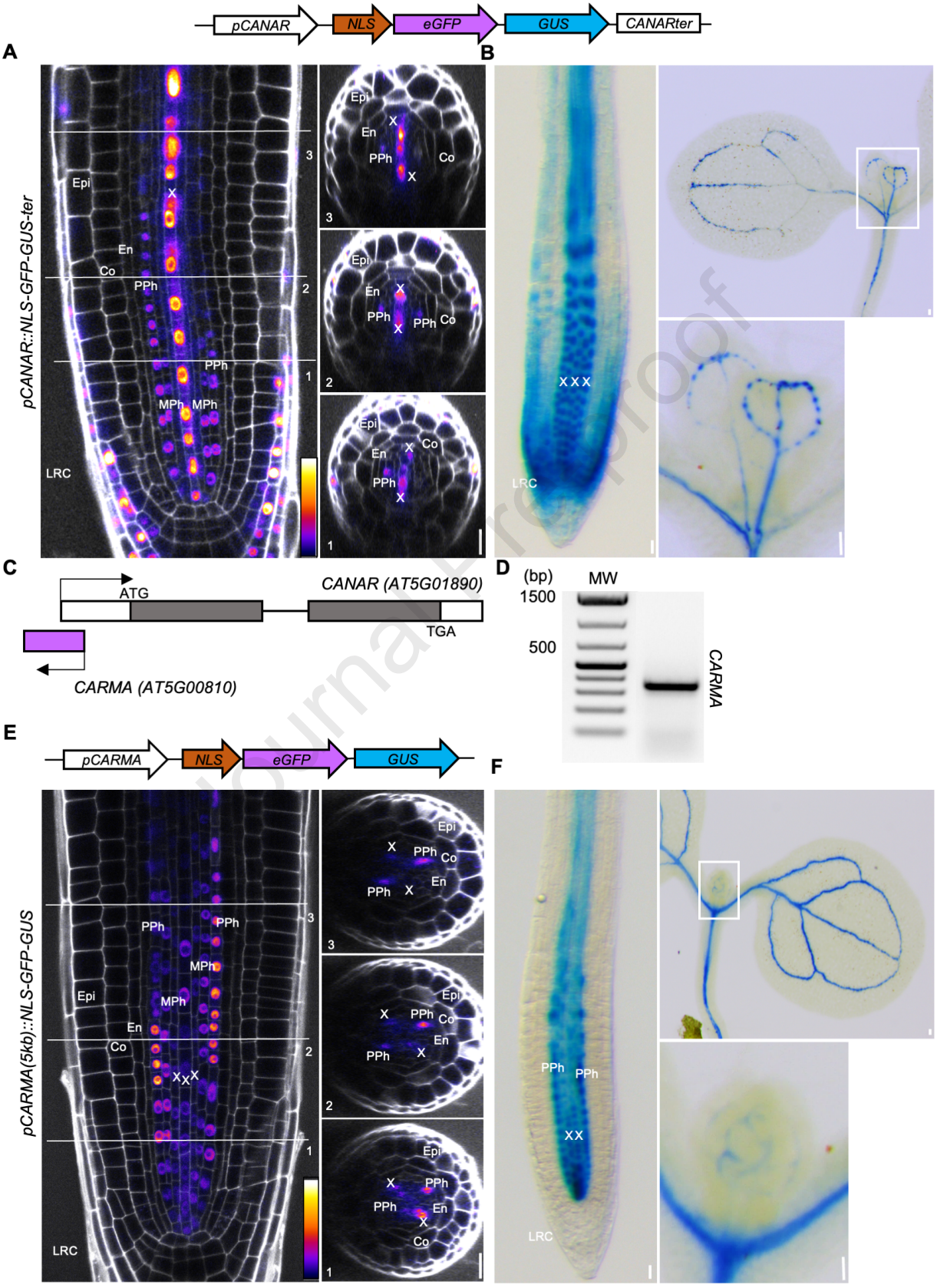
pCANAR
NLS
eGFP
GUS
CANARter
A
B
pCANAR::NLS-GFP-GUS-ter
Epi
En
Co
PPh
MPh
X
XXX
LRC
C
ATG
TGA
CANAR (AT5G01890)
CARMA (AT5G00810)
D
(bp)
MW
1500
500
CARMA
E
F
pCARMA
pCARMA(5kb)::NLS-GFP-GUS
XX

Fig.2

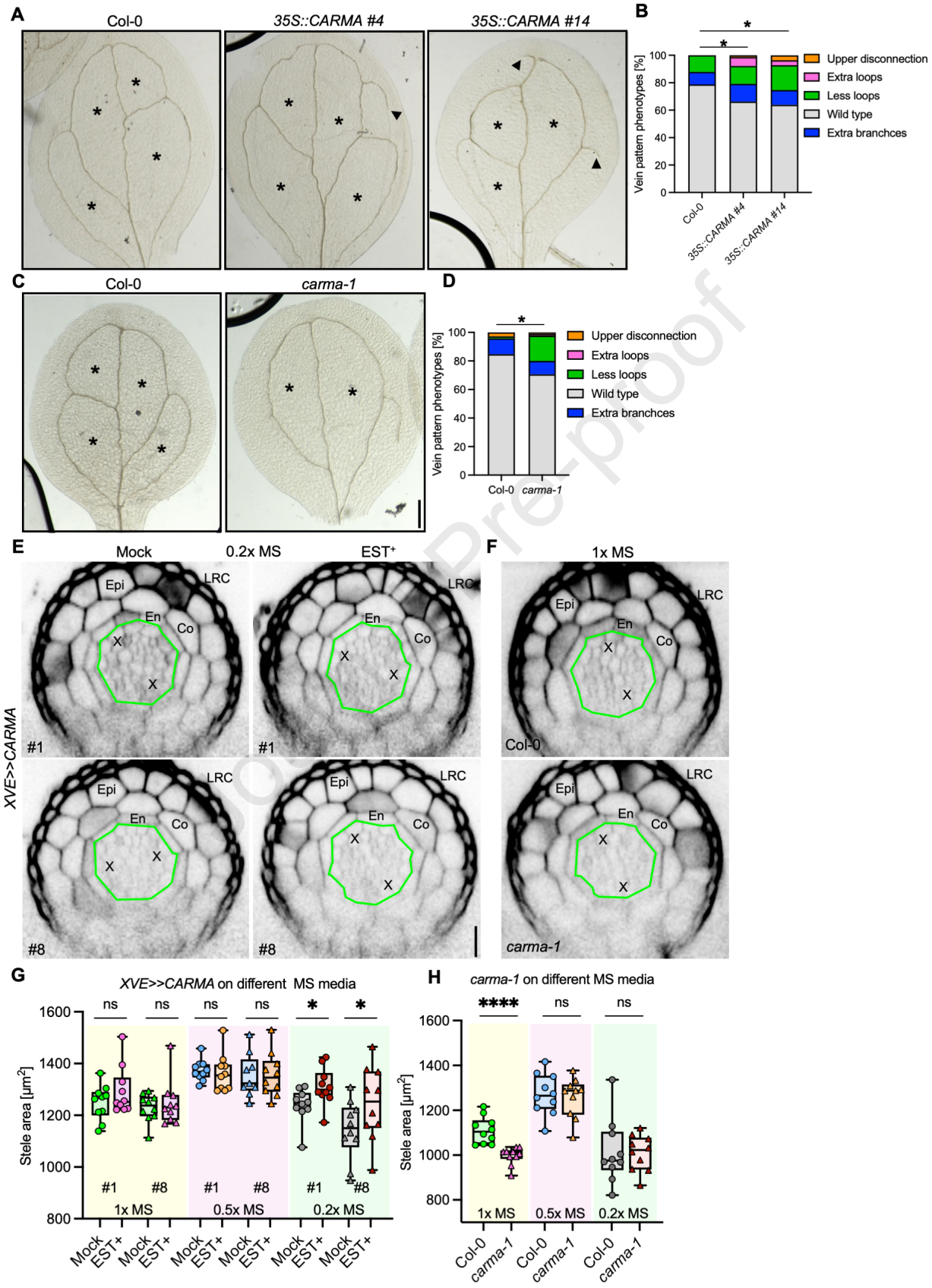
A
Col-0
35S::CARMA #4
35S::CARMA #14
B
Vein pattern phenotypes [%]
Upper disconnection
Extra loops
Less loops
Wild type
Extra branchces
Col-0
35S::CARMA #4
35S::CARMA #14
C
Col-0
carma-1
D
Vein pattern phenotypes [%]
Upper disconnection
Extra loops
Less loops
Wild type
Extra branchces
Col-0
carma-1
E
Mock
0.2x MS
EST+
XVE>>CARMA
Epi
LRC
En
Co
X
#1
#8
F
1x MS
Col-0
carma-1
G
XVE>>CARMA on different MS media
Stele area [µm²]
ns
*
#1
#8
1x MS
0.5x MS
0.2x MS
Mock
EST+
H
carma-1 on different MS media
****
ns
Stele area [µm²]
1x MS
0.5x MS
0.2x MS
Col-0
carma-1

Fig.3

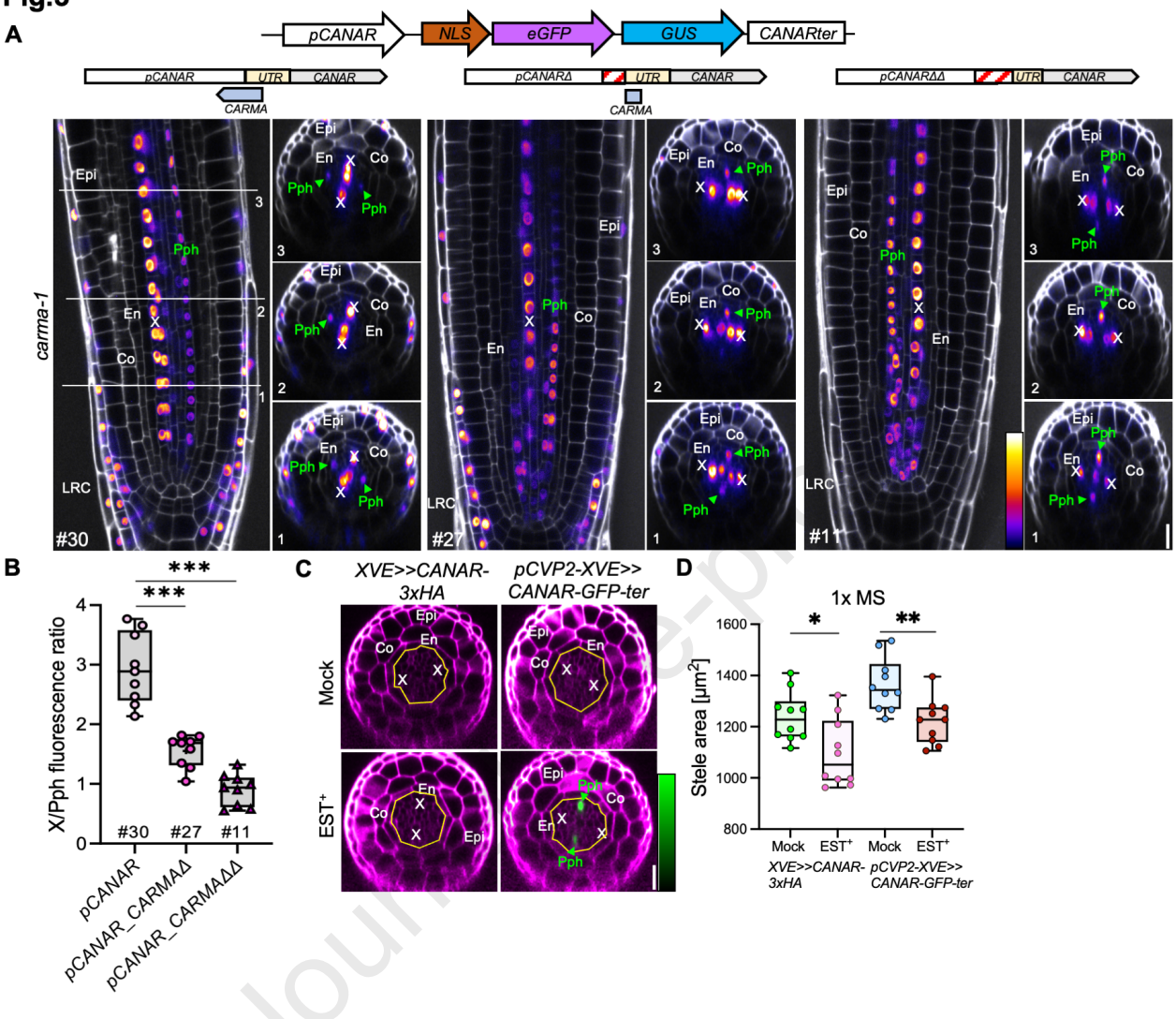
A
pCANAR
NLS
eGFP
GUS
CANARter
pCANAR
UTR
CANAR
CARMA
pCANARΔ
pCANARΔΔ
carma-1
Epi
Pph
En
Co
LRC
#30
#27
#11
B
X/Pph fluorescence ratio
***
pCANAR
pCANAR_CARMAΔ
pCANAR_CARMAΔΔ
C
XVE>>CANAR-3xHA
pCVP2-XVE>>CANAR-GFP-ter
Mock
EST+
D
1x MS
Stele area [µm2]
*
**
Mock
EST+
XVE>>CANAR-3xHA
pCVP2-XVE>>CANAR-GFP-ter

Fig.4

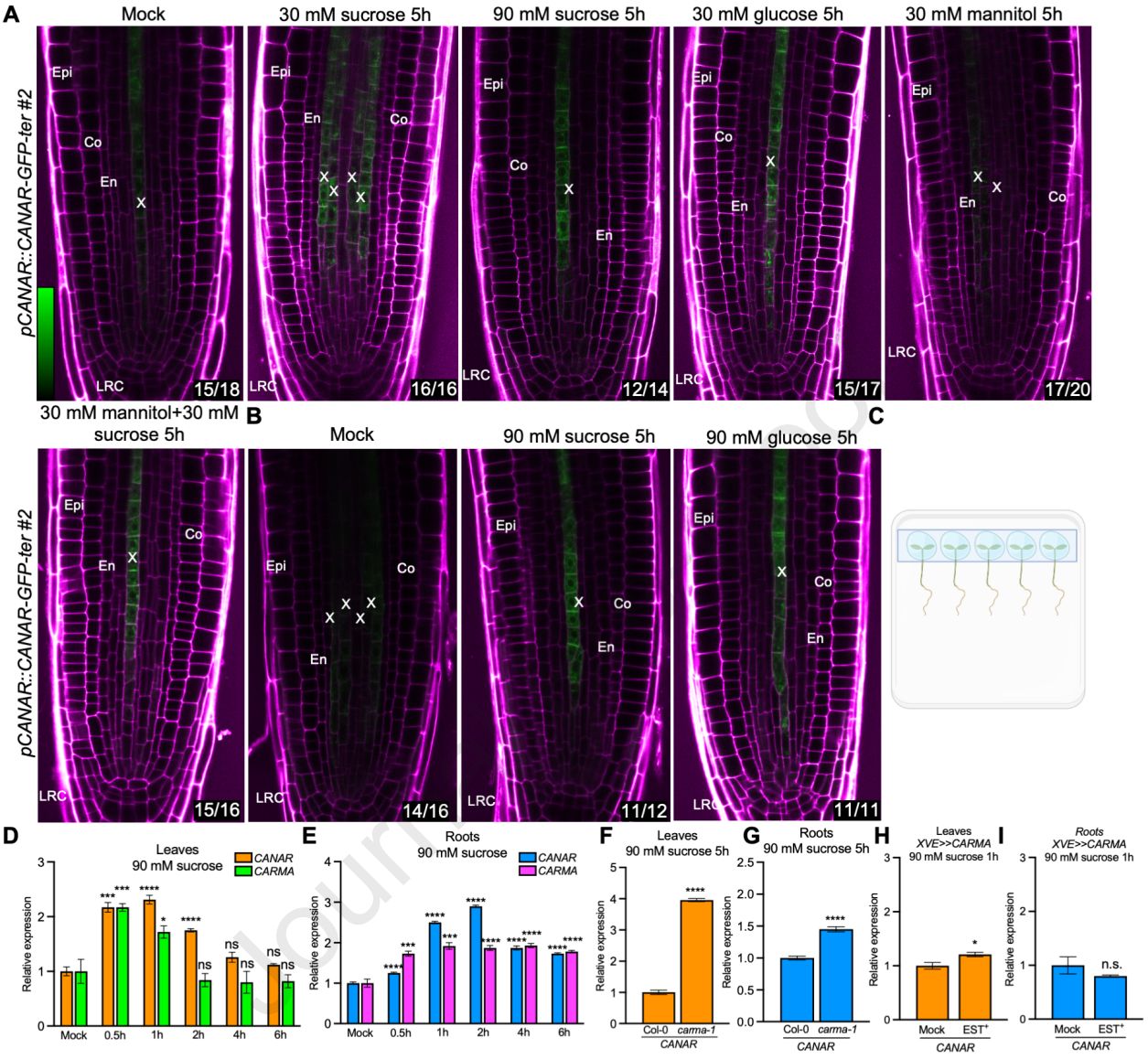
A
Mock
30 mM sucrose 5h
90 mM sucrose 5h
30 mM glucose 5h
30 mM mannitol 5h
pCANAR::CANAR-GFP-ter #2
Epi
Co
En
X
LRC
15/18
16/16
12/14
15/17
17/20
30 mM mannitol+30 mM sucrose 5h
B
Mock
90 mM sucrose 5h
90 mM glucose 5h
15/16
14/16
11/12
11/11
C
D
Leaves
90 mM sucrose
CANAR
CARMA
Relative expression
Mock
0.5h
1h
2h
4h
6h
E
Roots
90 mM sucrose
F
Leaves
90 mM sucrose 5h
Col-0
carma-1
G
Roots
90 mM sucrose 5h
H
Leaves
XVE>>CARMA
90 mM sucrose 1h
EST+
I
Roots
XVE>>CARMA
90 mM sucrose 1h
n.s.

Fig.5

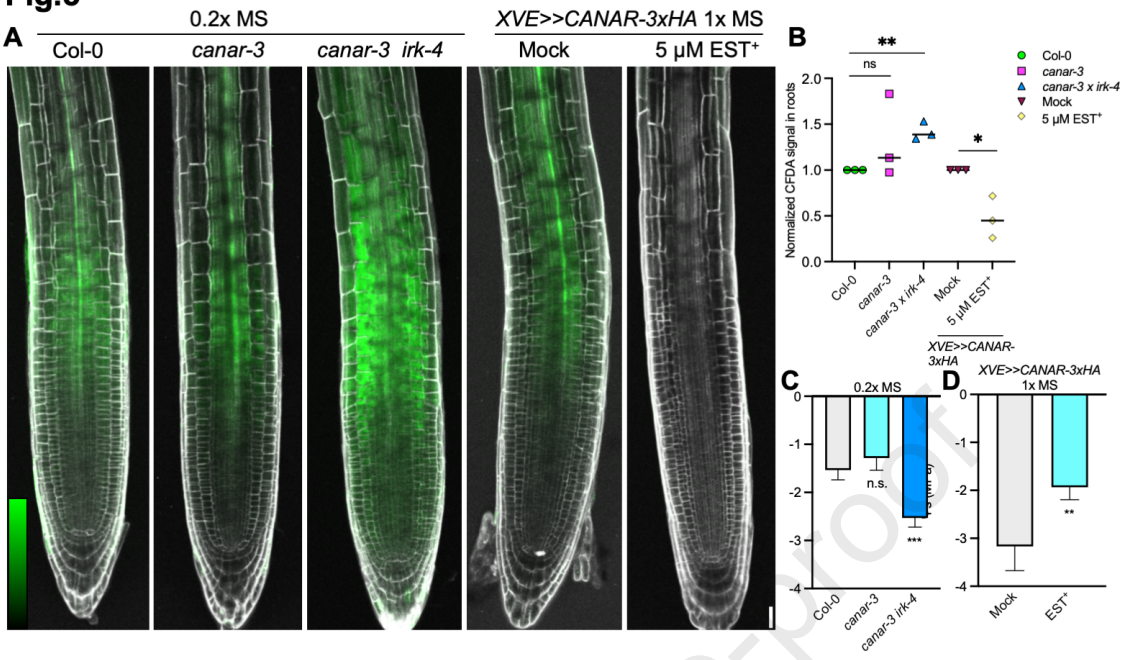

Fig. 6